



# Impurity sources and incorporation pathways during sputter deposition of Mg and Al thin films

Shamsa Aliramaji<sup>a</sup>, Philipp Keuter<sup>a</sup>, Stanislav Mráz<sup>a</sup>, Deborah Neuß<sup>a</sup>, Marcus Hans<sup>a</sup>, Daniel Primetzhofer<sup>b</sup>, Diederik Depla<sup>c</sup>, Jochen M. Schneider<sup>a,\*</sup>

<sup>a</sup> Materials Chemistry, RWTH Aachen University, Kopernikusstr. 10, 52074 Aachen, Germany

<sup>b</sup> Department of Physics and Astronomy, Uppsala University, Box 516, 75120 Uppsala, Sweden

<sup>c</sup> Department of Solid State Sciences, Ghent University, Krijgslaan 281 (S1), B-9000 Gent, Belgium

## ARTICLE INFO

### Keywords:

Impurity incorporation  
Physical vapor deposition (PVD)  
Thin film

## ABSTRACT

Minimizing the impurity concentration in magnetron sputter deposited thin films is desired for the exploration of composition – structure – property relations. Thus, the integral impurity incorporation during growth into Mg and Al sputter deposited thin films is studied by systematic variations of the base pressure, the deposition rate, and the working gas purity. The deposition rate and the base pressure, which was measured before each deposition, were varied simultaneously, resulting in a variation of the impurity-to-metal flux ratios of factor > 40. During growth, Ar gas purities of 99.999 and 99.9999 % were employed. Surprisingly, these systematic growth condition variations did not significantly alter the impurity concentration incorporated into Mg and Al thin films. While the modified parameters clearly are relevant for impurity incorporation, there appears to be at least one additional mechanism affecting the impurity incorporation during thin film growth operational. Mass spectrometry data revealed that residual gases desorb from surfaces within the vacuum chamber as soon as they are heated. Based on the measured thin film composition data, it is inferred that the magnitude of thermally desorbed residual gas appears to affect the impurity concentration to a larger extent than the systematic deposition parameter variations studied here. Therefore, it is reasonable to assume that the here investigated impurity incorporation is governed by the incorporation of thermally desorbed residual gases during thin film growth. Future impurity incorporation studies should, in addition to the base pressure before deposition, also quantify the residual gas partial pressures present during deposition.

## 1. Introduction

Venting the vacuum chamber exposes all surfaces to ambient air and gas adsorption is enabled [1]. During evacuation, the resulting pressure is affected by removal of gas by pumping, desorption, adsorption, as well as permeation [2]. In equilibrium, the gas desorption rate from the chamber walls depends on a variety of factors including the nature of the gas-surface-interaction [3], the amount of adsorbed and absorbed gases [4], and the temperature [5] and contributes to the base pressure, i.e., the pressure reached before processing is initiated. While baking, the increase in chamber surface temperature results in additional gas desorption enabling a reduction of the ultimate base pressure [1]. The remaining gas molecules and atoms present in the vacuum chamber are called residual gases [2,6]. During growth, the residual gases can be incorporated into the thin films [7] and may result in alteration of

interatomic bonding [8–11], thin film microstructure [12–18], and consequently also the film properties [16–20]. For example, a reduction in average binding energy was noted for amorphous Al<sub>2</sub>O<sub>3</sub> thin films in the presence of H, causing a decrease in its elastic modulus [9]. Moreover, it has been indicated that for SrTiO<sub>3</sub> an increase in H impurities results in the formation of non-ionic bonds, and thus strontium titanium oxide hydroxide forms instead [8]. Furthermore, the increase in O concentration in (V,Al)N and (Ti,Al)N and the concurrent replacement of N with O on the non-metal sublattice was shown to induce metal vacancies to attain charge neutrality, as well as larger transition metal-O bond length compared to metal-N bond length. Consequently, bond weakening and a lower elastic modulus are obtained [10,11]. The effect of impurities on thin film microstructure and, therefore, film properties has also been discussed in the literature. For example, incorporated impurities stemming from residual gases such as O and H<sub>2</sub>O have been

\* Corresponding author.

E-mail address: [schneider@mch.rwth-aachen.de](mailto:schneider@mch.rwth-aachen.de) (J.M. Schneider).

<https://doi.org/10.1016/j.surfcoat.2025.132216>

Received 25 April 2025; Accepted 26 April 2025

Available online 1 May 2025

0257-8972/© 2025 The Authors. Published by Elsevier B.V. This is an open access article under the CC BY license (<http://creativecommons.org/licenses/by/4.0/>).

shown to result in finer grains during growth of Al thin films [15]. Similarly, the presence of impurities in  $\text{Ni}_{90}\text{Cr}_{10}$  resulted in a decreased grain size which is ascribed to the increased number of nucleation sites facilitated by impurity incorporation [7]. Moreover, a more pronounced preferred orientation and porosity, as well as a lower defect density and film hardness was induced by O incorporation into (Ti,Al)N [16]. In another study, it was shown that the impurity-to-metal flux ratio effectively controls the texture, grain size, porosity, and elastic properties of nanocrystalline CoCrCuFeNi thin films [17]. Specifically, with increasing impurity-to-metal flux ratio, the grain size decreases, while the porosity was reported to increase [17]. Further effects of impurities on thin film properties have also been documented. For example, in Si thin films, the incorporation of O resulted in lower photosensitivity since O is positively ionized during normal solar cell operation, acts as an electron donor, and leads to the presence of undesirable free electrons before illumination [20]. In another study, partial oxidation of  $\text{Ni}_{83}\text{Fe}_{17}$  by residual gas incorporation was observed leading to a change in its magnetic properties [14].

All these examples demonstrate the impact of impurity incorporation on thin film properties, which are often undesirable from an application perspective as well as from a material science point of view, for exploring composition – structure – property relationships. Therefore, it is important to identify sources and incorporation pathways of impurities to avoid or at least reduce their incorporation.

Impurity incorporation occurs either during growth by interaction with residual gas or after growth, when the film is exposed to atmosphere [21]. Impurity incorporation by atmosphere exposure has been studied for Mg, Al, and Ca [22], where deposition temperature and atmosphere exposure time were systematically varied. Morphological modifications induced by variations in deposition temperature were reported. The film morphologies exhibiting the lowest O concentrations were reported at a homologous temperature of 0.4 for both Mg and Al thin films.

Furthermore, Ca was reported to chemically react with  $\text{H}_2\text{O}$  and transform to  $\text{Ca}(\text{OH})_2$  upon atmosphere exposure leading to the subsequent film delamination after a period of five days. Therefore, Al-capping was studied in an effort to prevent impurity incorporation through atmosphere exposure by depositing a 70 nm Al-capping on Mg and Ca thin films. Comparison of impurity concentrations in Al-capped and uncapped thin films demonstrated that Ca thin films are locally protected by Al-capping, whereas Mg (and Al) form self-passivation layers [22]. By considering the target, vacuum chamber, and working gas as the main sources of impurities, several factors may affect growth-related impurity incorporation during film growth such as target oxidation [23], target purity [24], deposition rate [25], base pressure [26] and working gas purity [19,26]. Selected influencing factors of impurity incorporation are further discussed below.

For conventional magnetron sputtering, a working gas is required and, in the case of reactive sputtering, a reactive gas is added additionally. The intentional introduction of these gases into the deposition chamber, already containing residual gases that have not been pumped, is accompanied by the unintentional introduction of impurity gases, which are present in the working and reactive gases. Examples of atmosphere related impurity gases are  $\text{H}_2\text{O}$ ,  $\text{CO}_2$ , CO,  $\text{O}_2$ , and  $\text{N}_2$ , where the magnitude thereof depends on the working and reactive gas purities. Naturally, these unintentionally introduced impurity gases may be incorporated during thin film growth [19,26].

In light of the above discussion, the base pressure is equal to the residual gas species present in the vacuum chamber [8,9,17,23]. These species can be directly incorporated as impurities into the film during synthesis and influence the process of film growth [27] and the film properties [9]. Kuo et al. investigated the effect of base pressure on hydrogenated amorphous silicon (a-Si:H) thin film synthesis by increasing it from  $1.3 \times 10^{-5}$  to  $1.3 \times 10^{-1}$  Pa ( $10^{-7}$  to  $10^{-3}$  Torr) and reported a higher O incorporation into the films with increasing the base pressure [28]. Furthermore, in the presence of magnetic fields, the field

strength thereof has a strong influence on the plasma composition [29]. Ionization of residual gases was shown to be magnetic field strength-dependent and the incorporation probability thereof in the film is larger than that of the neutral species [30].

Generally, the incorporation of residual gas species during thin film growth is related to the gas impingement flux ( $F_{\text{imp}}$ ), which expresses the number of gas atoms impinging on a unit surface area per unit time [5].  $F_{\text{imp}}$  can be estimated from the average speed of gas molecules based on the Maxwell-Boltzmann distribution. Assuming a uniform density of molecules,  $F_{\text{imp}}$  is given by:

$$F_{\text{imp}} = \frac{1}{4} n \langle v \rangle \quad (1)$$

where  $n$  is the gas (particle) density and  $\langle v \rangle$  is the average speed of gas molecules based on the Maxwell-Boltzmann distribution, which leads to the impingement flux:

$$F_{\text{imp}} = \frac{1}{4} n \sqrt{\frac{8k_B T}{\pi m}} \quad (2)$$

where  $k_B$  is Boltzmann's constant,  $T$  is absolute temperature, and  $m$  is the mass of the gas atom or molecule [3]. Using the ideal gas law and substituting

$$n = \frac{pN_A}{RT} \quad (3)$$

where  $p$  is the gas pressure,  $N_A$  is Avogadro's number ( $6.02 \times 10^{23}$  particles  $\text{mol}^{-1}$ ), and  $R$  is the universal gas constant ( $8.314 \text{ J mol}^{-1} \text{ K}^{-1}$ ), Eq. (2) becomes

$$F_{\text{imp}} = \frac{pN_A}{\sqrt{2\pi MRT}} \quad (4)$$

where  $M = m N_A$  is the molar mass of the considered gas. When assuming a sticking coefficient of 1, monolayer formation time  $\tau_c$  can be estimated based on:

$$\tau_c = \frac{B}{F_{\text{imp}}} = B \frac{\sqrt{2\pi MRT}}{pN_A} \quad (5)$$

where  $B$  is the number of atoms per unit area, which is assumed to be  $10^{19}$  atoms/ $\text{m}^2$  in one monolayer, and  $M$  is the molar mass of the residual gas, which is approximated by an averaged molar mass of O-containing species present in the residual atmosphere:  $\text{H}_2\text{O}$ ,  $\text{O}_2$ , CO, and  $\text{CO}_2$  ( $M = 30.5 \text{ g mol}^{-1}$ ) [5].

Similarly, the metal flux ( $F_m$ ) can be calculated using the following equation:

$$F_m = \frac{R_d \rho N_A}{M_m} \quad (6)$$

where  $R_d$ ,  $\rho$  (Mg  $1.738 \text{ g cm}^{-3}$ , Al  $2.7 \text{ g cm}^{-3}$ ), and  $M_m$  (Mg  $24.3 \text{ g mol}^{-1}$ , Al  $26.98 \text{ g mol}^{-1}$ ), are the deposition rate, mass density, and molar mass, respectively. The deposition rate is determined by dividing the film thickness by the time required for deposition. To quantify the relationship between deposition rate, metal flux, and impurity flux, knowledge of the sticking factors and the incorporation probabilities for each species is required [31,32]. The metal flux as well as the impurity flux influence the deposition rate as these species arrive at the substrate concurrently and contribute to the overall film growth. Hence, impurity incorporation is the result of a complex interplay between intentionally and unintentionally deposited fluxes.

Considering a deposition rate variation assuming a constant population of impurities in the gas phase and a constant impurity incorporation probability, the amount of incorporated impurities is expected to be lowered as the deposition rate is increased [17].

In the present work, various potential impurity sources as well as impurity incorporation pathways are systematically studied during the

synthesis of Mg and Al thin films. To allow for an investigation of solely growth-related impurity incorporation pathways, additional impurity uptake due to atmosphere exposure needs to be avoided [22]. Here, this is accomplished by self-passivation [22] and utilizing capping layers [21,22]. To this end, systematic variations in the base pressure, working gas purity, and deposition rate are compared to the measured impurity concentrations in Mg and Al thin films to identify impurity sources and incorporation pathways during sputtering.

## 2. Materials and methods

Thin film deposition was carried out by direct current magnetron sputtering in a high vacuum chamber using elemental targets of Mg (99.95 % as certified by MaTecK GmbH, < 80 ppm = 0.008 at.% of oxygen, 50.8 mm diameter) and Al (99.99 % as certified by Hydro Aluminium High Purity GmbH, 100 ppm = 0.01 at.% of oxygen, 50.8 mm diameter), respectively, on Si (100) substrates at floating potential at and target-to-substrate distance of 10 cm. The aforementioned oxygen concentrations were determined at a certified commercial materials analysis laboratory using carrier gas hot extraction (CGHO). The previously atmosphere-exposed Mg and Al targets were sputter cleaned at 200 W for a prolonged period (approx. 30 min) prior to each deposition series to ensure a clean target surface. Furthermore, sputter cleaning behind a shutter was done for 1 min at a deposition power between 50 and 200 W (Table 1) before each deposition. Prior to the initial deposition, the chamber was baked for 48 h at 100 °C using externally applied heating bands, followed by raising the temperature of the substrate heater to 460 °C for 2 h. Subsequently, the average chamber base pressure at room temperature was  $5.7 \pm 1.7 \times 10^{-6}$  Pa (measured by a hot cathode ionization Bayard-Alpert type pressure gauge integrated into an IONIVAC Transmitter ITR 200 S, Leybold) resulting in a monolayer formation time  $\tau_c$  of  $70 \pm 20$  s, respectively (see Eq. (5)). Subsequently, the substrates were heated to the deposition temperature of 100 °C, and after a heating dwell time of 20 min, the base pressure reached  $5.5 \pm 1.5 \times 10^{-6}$  Pa, equivalent to  $\tau_c$  of  $80 \pm 22$  s.

To study the impurity incorporation pathways and to identify impurity sources, the deposition parameters, working gas purity, base pressure, and deposition rate were varied systematically. While targets and gases constitute impurity sources, we have varied the Ar gas purity systematically and used Al and Mg targets with identical purity, supplying corresponding constant impurity fluxes. Gas purities of  $\geq 99.999$

% (5N) and  $\geq 99.9999$  % (6N) (Air Products GmbH) were used during the experiments. The gas lines were cleaned by flushing.







Single-layer thin films were deposited with varying working gas purities of  $\geq 5$ N and  $\geq 6$ N. At a total pressure of 0.5 Pa, where the total pressure is the sum of the Ar partial pressure plus the base pressure, the impurity partial pressures, introduced via the Ar, were calculated, based on the impurity information given by the supplier, to be  $\leq 5 \times 10^{-6}$  Pa (5N) and  $\leq 5 \times 10^{-7}$  Pa (6N). These contributions need to be added to the base pressure to calculate a combined  $\tau_c$  to consider the impurity contributions from the Ar as well as from the base pressure. Thus, at a deposition temperature of 100 °C and a base pressure of  $5.5 \pm 1.5 \times 10^{-6}$  Pa (resulting in a  $\tau_c$  of  $80 \pm 22$  s as described above), introducing Ar gas with a purity of  $\geq 5$ N results in a combined  $\tau_c$  of  $39 \pm 6$  s. Hence, the addition of the impurities contained in Ar with a purity of  $\geq 5$ N reduces the  $\tau_c$  by  $\geq 49 \pm 7$  %. Furthermore, at a deposition temperature of 100 °C and a base pressure of  $5.5 \pm 1.5 \times 10^{-6}$  Pa and therefore  $\tau_c$  of  $80 \pm 22$  s, introducing Ar gas with a purity of  $\geq 6$ N results in a combined  $\tau_c$  of  $72 \pm 18$  s. Thus, the addition of the impurities contained in Ar with a purity of  $\geq 6$ N reduces the  $\tau_c$  by  $9 \pm 2$  %. For details of the synthesis parameters see Table 1.

In a second set of experiments, 3-layered stacked thin films were synthesized using Ar with a purity of  $\geq 5$ N. Here, both the base pressure and deposition rate were kept constant within each individual layer but were varied from layer to layer. For the first and third deposited layers of the Mg stacked configuration, the base pressure was intentionally increased to  $5.0 \times 10^{-5}$  and  $6.0 \times 10^{-5}$  Pa, respectively. Similarly, for the Al stacked configuration, the base pressure was intentionally increased to  $5.5 \times 10^{-5}$  and  $4.0 \times 10^{-5}$  Pa, for the deposition of the first and third layers, respectively. This intentional increase in base pressure is accomplished by throttling the turbomolecular pump by partially closing a gate valve thereby reducing the combined  $\tau_c$  by an order of magnitude in both stacked thin film configurations. For the second layer, a base pressure of  $6.2 \times 10^{-6}$  Pa for Mg stack and of  $5.0 \times 10^{-6}$  Pa for Al stack was achieved by pumping with a completely open gate valve and therefore maximum pumping speed.

In the case of Mg, the ratio of base pressure to deposition rate of the first and third layers was  $9.3 \pm 0.9 \times 10^{-6}$  Pa min/nm while, this value dropped by two orders of magnitude to  $5.3 \times 10^{-8}$  Pa min/nm for the second layer corresponding to impurity-to-metal flux ratio of 0.003. Similarly, for Al, the ratio of base pressure to deposition rate was  $2.0 \pm 0.3 \times 10^{-5}$  Pa min/nm for the first and third layers, while the ratio

**Table 1**

Synthesis parameters of Mg and Al thin films and the corresponding combined monolayer formation times  $\tau_c$  at 100 °C considering both sources of impurities - the base pressure and the used Ar gas (5N refers to 99.999 %, while 6N refers to 99.9999 %). Layers 1, 2, and 3 in the stack configuration refer to the deposition sequence of the stack. Hence, layer 1 is deposited onto the substrate and layers 2 and 3 onto layers 1 and 2, respectively. The higher base pressure was achieved by throttling the vacuum pump.

Base pressure ( $\times 10^{-6}$ Pa)	Mg					Al				
	7.0	4.8	layer 3	layer 2	layer 1	4.0	4.5	layer 3	layer 2	layer 1
			60*	6.2	50*			40*	5.0	55*
Ar purity	5N	6N	5N	5N	5N	5N	6N	5N	5N	5N
$\tau_c$ (s)	34	76	6	36	7	45	81	9	40	7
DC target power (W)	50	50	10	200	10	200	200	20	200	20
Al-capping	Yes	Yes	No			No	No	No		
Configuration										

decreased by two orders of magnitude to  $2.0 \times 10^{-7}$  Pa min/nm in the second layer. This corresponds to impurity-to-metal flux ratio of 0.010 for layer 2 and 0.461 for layer 3. Thus, in both stacked thin film configurations, a significantly lower impurity content is expected in the second layer compared to the first and third layers.

Details of the synthesis parameters are summarized in Table 1. For the synthesis of all thin films, the substrate was rotated at 15–20 rpm. Al-capping layers with a thickness of approximately 70 nm were deposited onto selected thin films for 3 min at a temperature  $\leq 50$  °C at 200 W [22], see Table 1.

Chemical composition analysis was performed by energy dispersive X-ray spectroscopy (EDX) using an EDAX Genesis 2000 analyzer in a JEOL JSM 6480 scanning electron microscope. The acceleration voltage was set to 8 kV and the measurement time was 100 s at a magnification of 1000 $\times$ . Background deconvolution was optimized with respect to the O K $\alpha$  transition. Error bars correspond to standard deviations determined from 3 to 5 measurements of each sample. Chemical composition depth profiles were obtained with time-of-flight elastic recoil detection analysis (ToF-ERDA) at the Tandem Laboratory of Uppsala University [33]. 36 MeV  $^{127}\text{I}^{8+}$  primary ions were directed onto the thin films at an angle of 67.5° with incidence and exit angle of 22.5°. The time-of-flight measurement was carried out with thin C foils [34] and the time-energy coincidence spectra were converted to depth profiles with the CONTES software package [35]. The systematic uncertainty of 10 % relative to the deduced values for O and H originates from uncertainties of stopping powers from primary ions as well as the recoiling particles as discussed in the supplementary material of to Baben et al. [36]. Conversion of the areal density of depth profiles to nanometers was done using a measured density of 1.7 and 2.7 g cm $^{-3}$  for Mg [37] and Al [38], respectively. Error bars correspond to the standard error of the measured concentrations in the depth profiles of thin films excluding the surface.

The chamber pressure and residual gas composition were assessed using a hot cathode ionization Bayard-Alpert type pressure gauge, integrated into a Leybold IONIVAC Transmitter ITR 200 S, and a Pfeiffer Vacuum Prisma QME 200 residual gas analyzer (RGA), respectively. Hereby, the deposition scenario utilizing maximum pumping speed and the corresponding impurity incorporation resulting from heating during deposition caused by, for example, plasma ignition was mimicked. For this purpose, the chamber was baked out to reach a pressure of  $3.0 \times 10^{-7}$  Pa after cooling down to room temperature. Subsequently, changes in chamber pressure and gas composition, occurring during heating the substrate from room temperature to 100 °C, were monitored.

### 3. Results and discussion

To allow for a systematic study of impurity incorporation during thin film growth in the presence of residual gas, surface composition modification upon atmosphere exposure needs to be prevented [39]. In an effort to exclude chemical reactions with the atmosphere, selected films listed in Table 1 were capped. Our previous study showed that the Mg thin film surfaces form a self-passivating layer [22] and that the capping was not required. However, as the presence of the Al capping layer does not affect the conclusions drawn here, we decided against regrowing the capped films. Furthermore, it was previously [22] demonstrated that deposition temperature and, consequently, morphological modifications as well as evaporation, determine impurity incorporation by atmosphere exposure. Thus, in this study, a deposition temperature of 100 °C, corresponding to a homologous temperature of 0.4 for Mg and Al [23], was chosen, since the evolution of a dense microstructure was triggered by activation of both, surface and bulk diffusion, while desorption was avoided due to the low vapor pressure at this temperature [40,41].

#### 3.1. Working gas purity

The influence of working gas purity was investigated for Mg and Al thin films, where Ar with purities of  $\geq 5\text{N}$  and  $\geq 6\text{N}$  were used. The

impurity incorporation in Mg deposited in Ar with a purity of  $\geq 5\text{N}$  was taken from [22].

To study impurity incorporation, it is instructive to compare the ratio of impurity flux ( $F_{\text{imp}}$ ) to metal flux ( $F_{\text{m}}$ ). The impurity flux is calculated based on the kinetic gas theory using Eq. (4) and the metal flux is determined by Eq. (6) (see Section 1). Deposition rate, metal flux, impurity flux, and the averaged impurity concentrations in the films based on ToF-ERDA (Mg) and EDX (Mg and Al) are summarized in Table 2.

By increasing Ar purities from  $\geq 5\text{N}$  to  $\geq 6\text{N}$  for Mg, the impurity-to-metal flux ratio is decreased by 60 % from 0.010 to 0.004, see Table 2, however, ERDA measurements reveal identical average O and H concentrations of  $0.1 \pm 0.1$  and  $0.1 \pm 0.1$  at.%, respectively, for the corresponding Mg films. For this composition evaluation, the first 70 nm below the film surface were excluded since surface oxidation by atmosphere exposure [22] affects the chemical composition. Similarly, corresponding O concentrations of  $0.4 \pm 0.1$  and  $0.5 \pm 0.1$  at.% are determined with EDX.

In the case of Al, an increase in Ar purity from 5N to 6N results in an impurity-to-metal flux ratio decrease by 50 % from 0.008 to 0.004, respectively. Despite this variation, for the corresponding thin films similar O concentrations of  $0.1 \pm 0.1$  and  $0.3 \pm 0.1$  at.% are obtained by ERDA.

The fact that for the Al films grown with the 6N and 5N Ar purity result, within the measurement error, in similar O concentrations clearly shows that the impurity incorporation is not controlled by the purity of the Ar. Also, it can be concluded that the target purity does not control the impurity incorporation of the here-deposited Mg and Al thin films as the impurity concentration in the target is at least one order of magnitude lower than the minimum oxygen concentration measured in the corresponding films. However, it is reasonable to assume that impurities contained in the target as well as in the Ar contribute towards the measured impurity concentrations.

#### 3.2. Base pressure and deposition rate

Impurity incorporation is the result of the complex interplay between

**Table 2**

Deposition rate ( $R_d$ ), metal flux ( $F_{\text{m}}$ ), impurity flux ( $F_{\text{imp}}$ ), and averaged O and H concentrations of Al-capped Mg films (measured by ToF-ERDA) and of Al-capped Mg and Al films (measured by EDX) synthesized in Ar atmosphere exhibiting different purities. The base pressure ( $p_{\text{base}}$ ) at 100 °C was  $5.5 \pm 1.5 \times 10^{-6}$  Pa. Average O and H concentrations are measured by ERDA excluding 70 nm of the surface.

		Mg		Al	
Experimental conditions	$p_{\text{base}} (\times 10^{-6} \text{ Pa})$	7.0	4.8	4.0	4.5
	Argon purity	5N	6N	5N	6N
	P (W)	50	50	200	200
	Al capping	Yes	Yes	No	No
	$R_d$ (nm/min)	39.0	46.8	27.3	31.6
Calculations	$F_{\text{m}} (10^{17} \text{ ptcl./m}^2\text{s})$	279.9	335.8	274.1	317.3
	$F_{\text{imp}} (10^{17} \text{ ptcl./m}^2\text{s})$	1.2	0.1	1.2	0.1
	$F_{\text{imp}} (10^{17} \text{ ptcl./m}^2\text{s})$ from argon	1.7	1.2	1.0	1.1
	$F_{\text{imp}} (10^{17} \text{ ptcl./m}^2\text{s})$ from $p_{\text{base}}$	2.9	1.3	2.2	1.2
	$F_{\text{imp}} (10^{17} \text{ ptcl./m}^2\text{s})$ total				
Concentration	$F_{\text{imp}}/F_{\text{m}}$	0.010	0.004	0.008	0.004
	O (at.%)	$0.1 \pm$	$0.1 \pm$	$0.1 \pm$	$0.3 \pm$
	ERDA	0.1	0.1	0.1	0.1
	H (at.%)	$0.1 \pm$	$0.1 \pm$	$0.1 \pm$	$0.1 \pm$
	ERDA	0.1	0.1	0.1	0.1
	O (at.%) EDX	$0.4 \pm$	$0.5 \pm$	$0.5 \pm$	$0.7 \pm$
		0.1	0.1	0.1	0.1

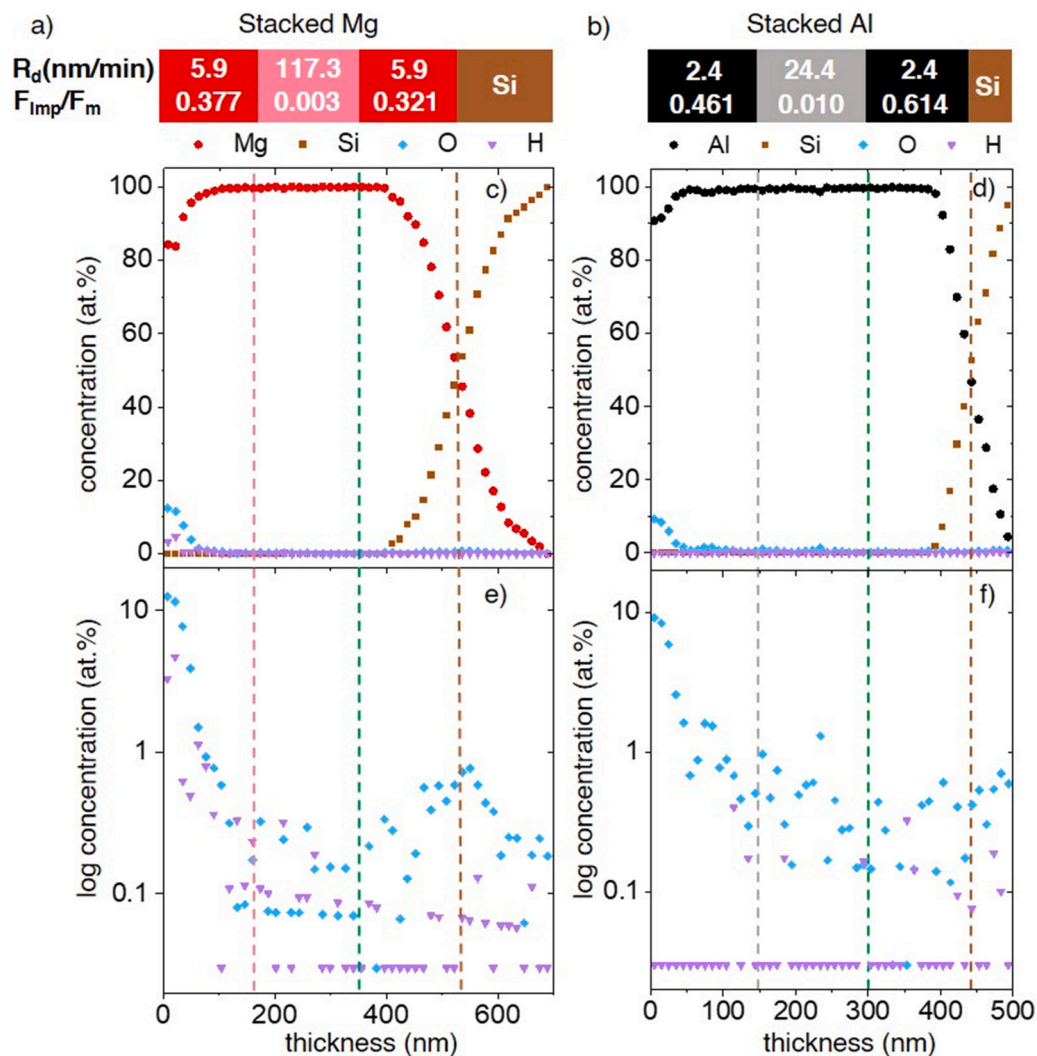


intentionally and unintentionally deposited fluxes of materials. Therefore, to determine the effect of the impurity-to-metal flux ratio on the impurity concentration, both, the base pressure, affecting the impurity flux, and the deposition rate, affecting the metal flux, are varied. Both variations are conducted within one deposition experiment utilizing configurations comprised of three individual layers. Each layer within the stack is deposited with different impurity-to-metal flux ratios as the deposition rate and the base pressure were varied see Fig. 1 a) and b). Within one layer, the base pressure and the deposition rate are kept constant, while in the next layer, the magnitude of both parameters is changed. For the deposition of the first and third layers, a low deposition rate is combined with a high base pressure, in an effort to maximize impurity incorporation. For the second layer, a high deposition rate is combined with a low base pressure, thereby minimizing impurity incorporation. As described in the experimental section, in the case of Mg, the ratio of base pressure to deposition rate of the first and third layers is  $9.3 \pm 0.9 \times 10^{-6}$  Pa min/nm while, this value is reduced by two orders of magnitude to  $5.3 \times 10^{-8}$  Pa min/nm for the second layer corresponding to impurity-to-metal flux ratio of 0.003. Similarly, for Al, this ratio is  $2.0 \pm 0.3 \times 10^{-5}$  Pa min/nm for the first and third layers while the ratio is decreased by two orders of magnitude to  $2.0 \times 10^{-7}$  Pa min/nm in the second layer. This corresponds to impurity-to-metal flux

ratio of 0.010 for layer 2 and 0.461 for layer 3. Chemical composition analysis conducted along the stack film thickness – through the various layers – was utilized to unravel the significance of the base pressure and deposition rate for the impurity incorporation during thin film growth.

To this end, ToF-ERDA depth profiling was performed, see Fig. 1 c) to f), and the corresponding metal and impurity fluxes were calculated in Table 3 using Eqs. (4) and (6) described in Section 1. Moreover, the O and H film concentrations measured by ToF-ERDA, excluding the 70 nm below the film surface, reported in Table 3 are averaged over each individual layer within the Mg and Al stacks. Layers 1, 2, and 3 refer to the deposition sequence of the stack. Hence, layer 1 is deposited onto the substrate and layers 2 and 3 onto layers 1 and 2, respectively.



As observed in Fig. 1 a) and b), and detailed in Table 3, the impurity-to-metal flux ratio of layer 1 (or 3) is with 0.321 (or 0.377) two orders of magnitude larger compared to layer 2 with an impurity-to-metal flux ratio of 0.003. Nevertheless, the measured O concentrations are  $0.1 \pm 0.1$ ,  $0.1 \pm 0.1$ , and  $0.3 \pm 0.1$  at.% for layers 1, 2, and 3, respectively, in the case of Mg. Moreover, irrespective of the impurity-to-metal flux ratio, H incorporation of  $0.1 \pm 0.1$  at.% is observed in all layers within the Mg stack. Hence, comparing the variation in impurity concentrations with the impurity-to-metal flux ratios of the individual layers assembled in Mg stack, see Table 3, with a constant oxygen flux of < 80 ppm from



**Fig. 1.** Schematics of stacked films deposited at 100 °C of a) Mg and b) Al. The impurity to metal flux ( $F_{imp}/F_m$ ) and deposition rate ( $R_d$ ) are shown for each layer of the stacks. ToF-ERDA composition depth profiles of c) and e) Mg; d) and f) Al thin films synthesized at varying base pressures and deposition rates. e) and f) show detailed information in logarithmic scale of O and H compositional depth profiles in c) and d), respectively. In instances where the concentration is zero, a value of 0.05 is depicted in Figures e) and f).

**Table 3**

Calculated metal flux ( $F_m$ ) and impurity flux ( $F_{imp}$ ), for each layer in Mg and Al stacked films. Averaged O and H concentrations are measured by ToF-ERDA excluding 70 nm of the surface. Layers 1, 2, and 3 are assembled from the substrate to the surface of the film, respectively.

		Mg			Al		
Experimental conditions		Layer 3	Layer 2	Layer 1	Layer 3	Layer 2	Layer 1
	p <sub>base</sub> (× 10 <sup>-6</sup> Pa)	60	6.2	50	40	5.0	55
	Argon purity	5N	5N	5N	5N	5N	5N
	DC target power	10	200	10	20	200	20
	Al capping	No			No		
	Configuration						
	R <sub>d</sub> (nm/min)	5.9	117.3	5.9	2.4	24.4	2.4
Calculations	F <sub>m</sub> (10 <sup>17</sup> ptcl./m <sup>2</sup> .s)	42.4	842.0	42.4	24.1	245.1	24.1
	F <sub>imp</sub> (10 <sup>17</sup> ptcl./m <sup>2</sup> .s) from argon	1.2	1.2	1.2	1.2	1.2	1.2
	F <sub>imp</sub> (10 <sup>17</sup> ptcl./m <sup>2</sup> .s) from p <sub>base</sub>	14.8	1.5	12.4	9.9	1.2	13.6
	F <sub>imp</sub> (10 <sup>17</sup> ptcl./m <sup>2</sup> .s) total	16.0	2.7	13.6	11.1	2.4	14.8
	F <sub>imp</sub> /F <sub>m</sub>	0.377	0.003	0.321	0.461	0.010	0.614
Concentration	O (at.%) ERDA	0.3 ± 0.1	0.1 ± 0.1	0.1 ± 0.1	0.8 ± 0.1	0.5 ± 0.1	0.2 ± 0.1
	H (at.%) ERDA	0.1 ± 0.1	0.1 ± 0.1	0.1 ± 0.1	0.1 ± 0.1	0.1 ± 0.1	0.1 ± 0.1

the target, it can be concluded that the systematic changes in deposition rate and base pressure studied here show no causal correlation with the O and H concentrations incorporated into the individual layers in the stack.

Regarding Al, the impurity-to-metal flux ratio of layer 1 (or 3) is with 0.614 (or 0.461) > 46 times larger compared to layer 2 with an impurity-to-metal flux ratio of 0.010. Despite this, the measured O concentrations in layers 1, 2, and 3 are  $0.2 \pm 0.1$ ,  $0.5 \pm 0.1$ , and  $0.8 \pm 0.1$  at.%, respectively. The oxygen flux from the target is with 100 ppm at least one order of magnitude lower than the concentration measured in the films. Moreover, irrespective of the impurity-to-metal flux ratio, H incorporation of  $0.1 \pm 0.1$  at.% is observed in all layers within the Al stack. As for the Mg stack discussed above, comparing the variation in impurity concentrations with the impurity-to-metal flux ratios of the individual layers assembled in Al stack, see Table 3, indicates that the systematic changes in deposition rate and base pressure performed here show no causal correlation with the O and H concentrations incorporated into the individual layers. Hence, it is reasonable to assume that at least one other, uncontrolled parameter affects the impurity incorporation during growth.

The measured O incorporation can be affected by the target purity [24], the gas purity [19,26], impurities in the gas lines [42], and of course the incorporated O from atmosphere exposure [22], which may proceed along the grain boundaries. While the target and gas purities were discussed previously, the gas lines, which were kept as short as possible, were prior to experiments flushed and thereby cleaned. Concerning the atmosphere exposure, it was shown previously for self-passivating Mg and Al thin films that O incorporation occurred over several days prior to passivation [22]. However, a previously overlooked incorporation pathway could be based on stimulated desorption. Indeed, it is plausible that desorption of residual gases from the reactor surfaces resulting from plasma surface interactions as well as indirect and direct

heating from heat sources could contribute to impurity incorporation during thin film growth. Thus, to critically appraise this hypothesis, the substrate heater was utilized as heat source causing desorption mimicking direct and indirect heating during plasma processing. The chamber pressure and the gas composition were continuously monitored using a hot cathode ionization Bayard-Alpert type pressure gauge (IONIVAC Transmitter ITR 200 S, Leybold) and a residual gas analyzer (Prisma QME 200, Pfeiffer Vacuum), respectively. Prior to this assessment, the chamber was baked out and, after cooling down to room temperature, a chamber pressure of  $3.0 \times 10^{-7}$  Pa was reached. Initially, the substrate was kept at room temperature for 10 min to establish baselines for the measured chamber pressure and RGA signals. Then, the heater was turned on and the substrate temperature was increased to 100 °C, maintained for 30 min and, subsequently, the heater was turned off. The corresponding temporal evolutions of the chamber pressure and H<sub>2</sub>O ion current are illustrated in Fig. 2. The H<sub>2</sub>O RGA signal is depicted here as it constitutes the most abundant residual gas species. The measured ion currents of the additional gas species are provided in Fig. S1 in the supplementary materials.

In Fig. 2, it is shown that as soon as the heater is turned on and the temperature increases from room temperature, the chamber pressure rises from  $3.0 \times 10^{-7}$  Pa by two orders of magnitude to a maximum of  $4.0 \times 10^{-5}$  Pa at 100 °C. Then, while the substrate temperature overshoots the 100 °C setpoint to 156 °C and subsequently decreases to 100 °C, the base pressure decreases and stabilizes at a pressure of  $1.2 \times 10^{-6}$  Pa which is close to the experimental base pressure with maximized pumping speed. Notably, as the chamber pressure is increased by heating, a corresponding rise in H<sub>2</sub>O ion current is measured with the RGA. A similar trend is observed for the other residual gases as shown in Fig. S1, indicating thermally stimulated desorption thereof. The concentration of H<sub>2</sub>O in the gas phase prior to heating is approximately 100 %. After heating for 8 min, the H<sub>2</sub>O signal decreases to 93 % while the

signals for CO/N and CO<sub>2</sub> increase to 4 and 3 %, respectively. As the substrate temperature is equilibrated at 100 °C (at 30 min) the concentration of H<sub>2</sub>O in the gas phase is again 100 %, indicating that H<sub>2</sub>O is preferentially desorbed and constitutes the only or the predominant species in the gas phase as surfaces within the vacuum chamber are heated. The measured signals for CO/N and CO<sub>2</sub> are below the detection limit except for the time intervals ranging from 11.5 to 13 and 15 to 23.5 min. It may be speculated that the first peak originates from desorbed species at the actual heating element, while the second peak is caused by desorption from the substrate heater component.

The initial chamber pressure utilized for the desorption measurements is with a pressure of  $3.0 \times 10^{-7}$  Pa one order of magnitude lower than the minimum base pressure obtained before the deposition of all the thin films, which ranged from  $4.0 \times 10^{-6}$  to  $6.0 \times 10^{-5}$  Pa. Thus, compared to the RGA data presented, the effect on the magnitude of gas desorption from chamber surfaces caused by, for example, direct and indirect heating as well as plasma-surface interactions, is expected to be even more pronounced in the growth experiments reported here due to the higher base pressure. It is reasonable to assume that the desorbed residual gases provide the feedstock for impurity incorporation during growth. As mentioned earlier, the systematic changes in deposition rate and base pressure studied here show no causal correlation with the O and H concentrations incorporated during growth. Thus, it is inferred that the magnitude of desorbed residual gases (here, primarily H<sub>2</sub>O, from the reactor surfaces, as illustrated by the here presented RGA data), resulting from plasma surface interactions, indirect and direct heating from the plasma sources as well as substrate heater has a more significant effect on the impurity concentration than the systematic deposition parameter variations. Based on these findings, future investigations into impurity incorporation should not only assess the base pressure prior to deposition but also quantify the partial pressures of residual gases during the deposition process.

#### 4. Conclusions

The goal of this study was to contribute towards a better understanding of the impurity incorporation pathways active during growth of Mg and Al thin films synthesized by magnetron sputtering to subsequently be able to improve film purity. For this purpose, the influence of impurity uptake relevant deposition parameters, such as the working gas purity, the base pressure, measured before deposition, as well as the deposition rate, were varied. Al and Mg thin film growth conducted with Ar gas purities of 5N and 6N did not result in a significant difference in impurity concentrations as revealed by ToF-ERDA and EDX data. Moreover, deposition rate and base pressure were varied simultaneously, leading to a variation in impurity-to-metal flux ratio of > factor 40. While no significant impurity concentration variation was revealed by ToF-ERDA data, mass spectrometry data illustrated that residual gases desorb from surfaces in the vacuum chamber as they are heated. Hence, it is inferred that the magnitude of thermally desorbed residual gases affect the impurity concentration to a larger extent than the systematic deposition parameter variations studied here, even at a base pressure in the ultra-high vacuum range.

Based on these findings, future investigations into impurity incorporation should not only assess the base pressure prior to deposition but also quantify the partial pressures of residual gases during the deposition process.

Supplementary data to this article can be found online at <https://doi.org/10.1016/j.surfcoat.2025.132216>.

#### CRediT authorship contribution statement

**Shamsa Aliramaji:** Conceptualization, Data curation, Formal analysis, Funding acquisition, Investigation, Methodology, Validation, Visualization, Writing – original draft, Writing – review & editing. **Philipp Keuter:** Data curation, Formal analysis, Investigation, Writing –

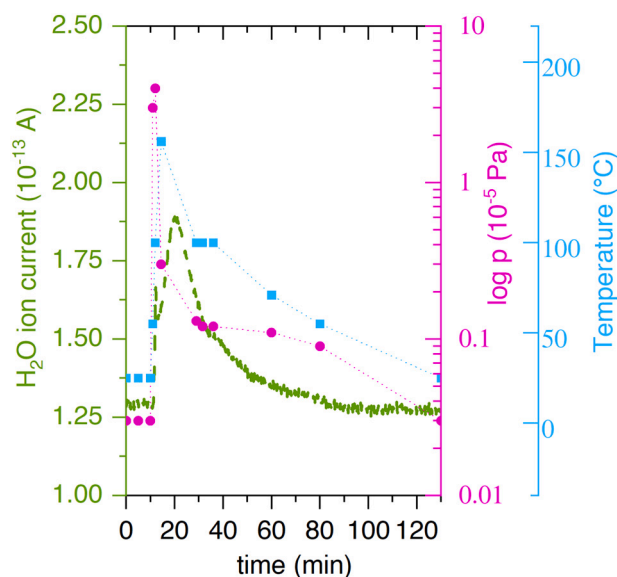


**Fig. 2.** Temporal evolution of chamber pressure and the H<sub>2</sub>O ion current from RGA measurements during heating of the substrate from room temperature to 100 °C.

review & editing. **Stanislav Mráz:** Data curation, Formal analysis, Investigation, Methodology, Supervision, Writing – review & editing. **Deborah Neuß:** Data curation, Formal analysis, Investigation, Writing – review & editing. **Marcus Hans:** Data curation, Formal analysis, Investigation, Writing – review & editing. **Daniel Primetzhofer:** Data curation, Formal analysis, Funding acquisition, Investigation, Methodology, Writing – review & editing. **Diederik Depla:** Supervision, Validation, Writing – review & editing. **Jochen M. Schneider:** Conceptualization, Project administration, Resources, Supervision, Validation, Writing – original draft, Writing – review & editing.

#### Declaration of competing interest

The authors declare that they have no known competing financial interests or personal relationships that could have appeared to influence the work reported in this paper.

#### Acknowledgments

This work was supported by Deutsche Forschungsgemeinschaft (DFG) within the Collaborative Research Center SFB 1394 “Structural and Chemical Atomic Complexity - From Defect Phase Diagrams to Materials Properties”, (project ID 409476157). Accelerator operation at Uppsala University was supported by the Swedish Research Council VR-RFI (Contract No. 2017-00646\_9) and the Swedish Foundation for Strategic Research (Contract No. RIF14-0053).

#### Data availability

Data will be made available on request.

#### References

- [1] J.F. O'Hanlon, *A User's Guide to Vacuum Technology*, John Wiley & Sons, Inc., 2003.
- [2] K. Jousten, *Handbook of Vacuum Technology*, Wiley-VCH Verlag GmbH & Co, KGaA, 2016.
- [3] P. Chiggiato, Vacuum technology for ion sources, in: Cern, 2014, pp. 463–502, <https://doi.org/10.5170/CERN-2013-007.463>.
- [4] A.H. Beck, *Handbook of Vacuum Physics*, 1964, <https://doi.org/10.1088/0031-9112/16/8/008>.
- [5] M. Ohring, *The Materials Science of Thin Films*, Academic Press, 1992.

- [6] O.B. Malyshev, *Vacuum in Particle Accelerators*, Wiley-VCH Verlag GmbH & Co, KGaA, 2020.
- [7] F.G. Coughnon, A. Dulmaa, R. Dedoncker, R. Galbadrak, D. Depla, Impurity dominated thin film growth, *Appl. Phys. Lett.* 112 (2018) 221903, <https://doi.org/10.1063/1.5021528>.
- [8] J.M. Schneider, B. Hjörvarsson, X. Wang, L. Hultman, On the effect of hydrogen incorporation in strontium titanate layers grown by high vacuum magnetron sputtering, *Appl. Phys. Lett.* 75 (1999) 3476–3478, <https://doi.org/10.1063/1.125301>.
- [9] J.M. Schneider, K. Larsson, J. Lu, E. Olsson, B. Hjörvarsson, Role of hydrogen for the elastic properties of alumina thin films, *Appl. Phys. Lett.* 80 (2002) 1144–1146, <https://doi.org/10.1063/1.1448389>.
- [10] K.P. Shaha, H. Rueß, S. Rotert, M. to Baben, D. Music, J.M. Schneider, Nonmetal sublattice population induced defect structure in transition metal aluminum oxynitrides, *Appl. Phys. Lett.* 103 (2013) 22–27, <https://doi.org/10.1063/1.4833835>.
- [11] M. Hans, M. To Baben, D. Music, J. Ebenhöch, D. Primetzhofer, D. Kurapov, M. Arndt, H. Rudigier, J.M. Schneider, Effect of oxygen incorporation on the structure and elasticity of Ti-Al-O-N coatings synthesized by cathodic arc and high power pulsed magnetron sputtering, *J. Appl. Phys.* 116 (2014) 093515, <https://doi.org/10.1063/1.4894776>.
- [12] P.B. Barna, M. Adamik, Fundamental structure forming phenomena of polycrystalline films and the structure zone models, *Thin Solid Films* 317 (1998) 27–33, [https://doi.org/10.1016/S0040-6090\(97\)00503-8](https://doi.org/10.1016/S0040-6090(97)00503-8).
- [13] M. Adamik, P.B. Barna, I. Tomov, Correlation between texture and average grain size in polycrystalline Ag thin films, *Thin Solid Films* 359 (2000) 33–38, [https://doi.org/10.1016/S0040-6090\(99\)00691-4](https://doi.org/10.1016/S0040-6090(99)00691-4).
- [14] P. Chowdhury, H.C. Barshilia, K.S. Rajam, P.K. Mishra, C.L. Prajapat, D.V. Sridhara Rao, Role of oxygen impurity in growth and magnetic properties of Ni<sub>83</sub>Fe<sub>17</sub> permalloy thin films, *J. Magn. Magn. Mater.* 322 (2010) 3266–3270, <https://doi.org/10.1016/j.jmmm.2010.06.005>.
- [15] P.B. Barna, G. Radnóczy, Structure formation during deposition of polycrystalline metallic thin films, in: *Met. Film. Electron. Opt. Magn. Appl.*, Elsevier, 2014, pp. 67–120, <https://doi.org/10.1533/9780857096296.1.67>.
- [16] H. Riedl, C.M. Koller, F. Munnik, H. Hutter, F. Mendez Martin, R. Rachbauer, S. Kolozsvári, M. Bartosik, P.H. Mayrhofer, Influence of oxygen impurities on growth morphology, structure and mechanical properties of Ti-Al-N thin films, *Thin Solid Films* 603 (2016) 39–49, <https://doi.org/10.1016/j.tsf.2016.01.039>.
- [17] B.R. Braeckman, P. Djemia, F. Tétard, L. Belliard, D. Depla, Impurity-controlled film growth and elastic properties of CoCrCuFeNi thin films, *Surf. Coat. Technol.* 315 (2017) 475–483, <https://doi.org/10.1016/j.surfcoat.2017.03.014>.
- [18] F. Coughnon, D. Depla, The Seebeck coefficient of sputter deposited metallic thin films: The role of process conditions, *Coatings* 9 (2019) 299, <https://doi.org/10.3390/coatings9050299>.
- [19] M. Takahashi, M. Tsunoda, H. Shoji, Ultra-clean sputtering process for magnetic thin films on hard disk drives, *Vacuum* 59 (2000) 814–824, [https://doi.org/10.1016/S0042-207X\(00\)00352-3](https://doi.org/10.1016/S0042-207X(00)00352-3).
- [20] T. Tabuchi, Y. Toyoshima, M. Takashiri, Effect of reducing impurity concentration of microcrystalline silicon thin films for solar cells using radio frequency hollow electrode enhanced glow plasma, *Vacuum* 101 (2014) 125–129, <https://doi.org/10.1016/j.vacuum.2013.08.002>.
- [21] P. Keuter, A.L. Ravensburg, M. Hans, S.K. Aghda, D.M. Holzapfel, D. Primetzhofer, J.M. Schneider, A proposal for a composite with temperature-independent thermophysical properties: HfV<sub>2</sub>-HfV<sub>2</sub>O<sub>7</sub>, *Materials (Basel)* 13 (2020) 5021, <https://doi.org/10.3390/ma13215021>.
- [22] S. Aliramaji, P. Keuter, D. Neuß, M. Hans, D. Primetzhofer, D. Depla, J. M. Schneider, Effect of growth temperature and atmosphere exposure time on impurity incorporation in sputtered Mg, Al, and Ca thin films, *Materials (Basel)* 16 (2022) 414, <https://doi.org/10.3390/ma16010414>.
- [23] J.M. Schneider, A. Anders, B. Hjörvarsson, I. Petrov, K. Macák, U. Helmersson, J.-E. Sundgren, Hydrogen uptake in alumina thin films synthesized from an aluminum plasma stream in an oxygen ambient, *Appl. Phys. Lett.* 74 (1999) 200–202, <https://doi.org/10.1063/1.123292>.
- [24] M. Moriyama, T. Morita, S. Tsukimoto, M. Shimada, M. Murakami, The effect of target purities on grain growth in sputtered copper thin films, *Mater. Trans.* 46 (2005) 1036–1041.
- [25] F.G. Coughnon, I.C. Schramm, D. Depla, On the electrical properties of sputter deposited thin films: The role of energy and impurity flux, *Thin Solid Films* 690 (2019) 137540, <https://doi.org/10.1016/j.tsf.2019.137540>.
- [26] M. Andritschky, Origin of gas impurities in sputtering plasmas during thin film deposition, *Vacuum* 42 (1991) 753–756, [https://doi.org/10.1016/0042-207X\(91\)90173-G](https://doi.org/10.1016/0042-207X(91)90173-G).
- [27] I. Petrov, P.B. Barna, L. Hultman, J.E. Greene, Microstructural evolution during film growth, *J. Vac. Sci. Technol. A* 21 (2003) S117–S128, <https://doi.org/10.1116/1.1601610>.
- [28] T.C. Kuo, Y.L. Jiang, Residual impurities in a process chamber on the characteristics of a-Si:H solar cells, *Sol. Energy Mater. Sol. Cells* 117 (2013) 617–623, <https://doi.org/10.1016/j.solmat.2013.07.052>.
- [29] J.M. Schneider, A. Anders, B. Hjörvarsson, L. Hultman, Magnetic-field-dependent plasma composition of a pulsed arc in a high-vacuum ambient, *Appl. Phys. Lett.* 76 (2000) 1531–1533, <https://doi.org/10.1063/1.126086>.
- [30] J.M. Schneider, A. Anders, G.Y. Yushkov, Magnetic-field-dependent plasma composition of a pulsed aluminum arc in an oxygen ambient, *Appl. Phys. Lett.* 78 (2001) 150–152, <https://doi.org/10.1063/1.1339847>.
- [31] Nagamitsu Yoshimura, *Vacuum Technology*, Springer Berlin Heidelberg, Berlin, Heidelberg, 2008, <https://doi.org/10.1007/978-3-540-74433-7>.
- [32] S. Mahieu, K. Van Aeken, D. Depla, D. Smeets, A. Vantomme, Dependence of the sticking coefficient of sputtered atoms on the target-substrate distance, *J. Phys. D Appl. Phys.* 41 (2008), <https://doi.org/10.1088/0022-3727/41/15/152005>.
- [33] P. Ström, D. Primetzhofer, Ion beam tools for nondestructive in-situ and in-operando composition analysis and modification of materials at the Tandem Laboratory in Uppsala, *J. Instrum.* 17 (2022) P04011, <https://doi.org/10.1088/1748-0221/17/04/P04011>.
- [34] Y. Zhang, H.J. Whitlow, T. Winzell, I.F. Bubb, T. Sajavaara, K. Arstila, J. Keinonen, Detection efficiency of time-of-flight energy elastic recoil detection analysis systems, *Nucl. Instruments Methods Phys. Res. Sect. B Beam Interact. with Mater. Atoms.* 149 (1999) 477–489, [https://doi.org/10.1016/S0168-583X\(98\)00963-X](https://doi.org/10.1016/S0168-583X(98)00963-X).
- [35] Jansson, M.S. Contes Instruction Manual; Uppsala University: Uppsala, Sweden, 2004., in: n.d.
- [36] M. to Baben, M. Hans, D. Primetzhofer, S. Evertz, H. Ruess, J.M. Schneider, Unprecedented thermal stability of inherently metastable titanium aluminum nitride by point defect engineering, *Mater. Res. Lett.* 5 (2017) 158–169, <https://doi.org/10.1080/21663831.2016.1233914>.
- [37] R.N. Abdullaev, R.A. Khairulin, Y.M. Kozlovskii, A.S. Agazhanov, S.V. Stankus, Density of magnesium and magnesium-lithium alloys in solid and liquid states, *Trans. Nonferrous Met. Soc. China.* 29 (2019) 507–514, [https://doi.org/10.1016/S1003-6326\(19\)64959-9](https://doi.org/10.1016/S1003-6326(19)64959-9).
- [38] A.R. Kurochkin, P.S. Popel', D.A. Yagodin, A.V. Borisenko, A.V. Okhapkin, Density of copper-aluminum alloys at temperatures up to 1400 °C determined by the gamma-ray technique, *High Temp.* 51 (2013) 197–205, <https://doi.org/10.1134/S0018151X13020120>.
- [39] G. Greczynski, S. Mráz, L. Hultman, J.M. Schneider, Venting temperature determines surface chemistry of magnetron sputtered TiN films, *Appl. Phys. Lett.* 108 (2016) 1–5, <https://doi.org/10.1063/1.4940974>.
- [40] P. Keuter, S.K. Aghda, D. Music, P. Kümmerl, J.M. Schneider, S. Karimi Aghda, D. Music, P. Kümmerl, J.M. Schneider, Synthesis of intermetallic (Mg<sub>1-x</sub>Al<sub>x</sub>)<sub>2</sub>Ca by combinatorial sputtering, *Materials (Basel)* 12 (2019) 3026, <https://doi.org/10.3390/ma12183026>.
- [41] P. Keuter, M. to Baben, S. Aliramaji, J.M. Schneider, CALPHAD-based modelling of the temperature-composition-structure relationship during physical vapor deposition of Mg-Ca thin films, *Materials (Basel)* 16 (2023) 2417, <https://doi.org/10.3390/ma16062417>.
- [42] T. Merdzhanova, J. Woerdenweber, W. Beyer, T. Kilper, U. Zastrow, M. Meier, H. Stiebig, A. Gordijn, Impurities in thin-film silicon: influence on material properties and solar cell performance, *J. Non Cryst. Solids* 358 (2012) 2171–2178, <https://doi.org/10.1016/j.jnoncrysol.2011.11.030>.